GEOPHYSICS, VOL. 87, NO. 3 (MAY-JUNE 2022); P. R291–R304, 20 FIGS.
10.1190/GEO2021-0097.1

DOI:10.1190/geo2021-0097.1

Waveform inversion of seismic first arrivals acquired on irregular surface

Xiang Li[1], Gang Yao[2], Fenglin Niu[1], Di Wu[3], and Nengchao Liu[3]

ABSTRACT

The irregular topography of the earth's surface and low signal-to-noise ratios of land seismic data bring challenges to full-waveform inversion (FWI). We propose a robust method for waveform inversion (WI) to invert such land seismic data. The inversion uses finite-difference methods with rectangular meshes to simulate seismic wavefields efficiently. To accurately model irregular free surface topography, we use an improved immersed boundary method with an iterative symmetric interpolation. First-arrival signals including direct waves and refraction waves are used to estimate the P-wave velocity. To overcome the cycle skipping and dynamic inconsistency issues between the modeled data and the observed data, we create an intermediate data set by shifting the first arrivals of the predicted data toward that of the observed data within half a cycle. The intermediate data instead of the observed data are then inverted. Thus, the inversion essentially matches the traveltime information of first arrivals, which is the most reliable information contained in seismic data. Applications on the synthetic and field data sets demonstrate that the proposed WI algorithm is robust for recovering P-wave velocity from land seismic data. The resulting models have higher resolution and deeper support than that of ray-based traveltime tomography.

INTRODUCTION

Full-waveform inversion (FWI) aims to recover elastic properties of the rocks by minimizing a misfit function that measures the difference between the simulated seismic data and observed data. When the simulated seismic wavefield data match the observed seismic wavefield data in terms of the defined misfit function, the inverted model is presumed to represent the real physical properties underground (Tarantola and Valette, 1982; Tarantola, 1984, 1986; Pratt, 1999; Tromp et al., 2005; Tromp, 2019; Yao et al., 2020a). To date, FWI has achieved numerous successes on marine seismic data applications (e.g., Sirgue et al., 2010; Warner et al., 2013; Jiao et al., 2015; Ramos-Martinez et al., 2016; Shen et al., 2017; Cobo et al., 2018; Zhang et al., 2020). There are two main reasons for the existing successes of FWI with marine seismic data. First, the acoustic assumption, which is widely used in FWI, is a reasonable assumption when modeling marine data due to seawater filtering out the elastic effects of seismic data. Second, marine seismic surveys usually provide relatively reliable waveform information due to high signal-to-noise ratio (S/N). In contrast, land seismic data are naturally elastic, comprising not only P waves but also S and surface waves. Furthermore, land seismic data are acquired on an irregular surface that tends to increase the complexity of the elastic wavefield due to reflections, conversion, and scattering (e.g., Hayashi et al., 2001; Zhang and Chen, 2006; Lombard et al., 2008; Rao and Wang, 2013, 2018; Hu, 2016). These two aspects, as well as other factors, impose great challenges for successful applications of FWI on land seismic data (e.g., Baeten et al., 2013; Stopin et al., 2014; Mei and Tong, 2015; Cheng et al., 2017; Sedova et al., 2019; Borisov et al., 2020).

Another effective velocity building method is the ray-based traveltime tomography method. It uses ray-tracing methods to calculate traveltime based on Fermat's principle. The classical ray-tracing methods include the shooting method (Langan et al., 1985), the bending method (Um and Thurber, 1987; Zhao et al., 1992), the eikonal equation method (Vidale, 1988; Qin et al., 1992), and the shortest raypath method (Moser, 1991). As a nonlinear optimization problem, traveltime tomography is solved by linearization of the nonlinear problem iteratively (Hole, 1992; Zelt and Smith,

Manuscript received by the Editor 7 February 2021; revised manuscript received 25 January 2022; published ahead of production 28 February 2022; published online 4 April 2022.
[1]China University of Petroleum (Beijing), State Key Laboratory of Petroleum Resources and Prospecting, Beijing, China; China University of Petroleum (Beijing), Unconventional Petroleum Research Institute, Beijing, China; and Rice University, Department of Earth, Environmental and Planetary Sciences, Houston, Texas, USA. E-mail: lixiang_cdut@163.com; niu@rice.edu.
[2]China University of Petroleum (Beijing), State Key Laboratory of Petroleum Resources and Prospecting, Beijing, China and China University of Petroleum (Beijing), Unconventional Petroleum Research Institute, Beijing, China. E-mail: yaogang@cup.edu.cn (corresponding author).
[3]China University of Petroleum (Beijing), State Key Laboratory of Petroleum Resources and Prospecting, Beijing, China and China University of Petroleum (Beijing), College of Geophysics, Beijing, China. E-mail: wudi@cup.edu.cn; lnengchao@qq.com.

DOI:10.1190/geo2021-0097.1

1992; Zhao et al., 1992; Hole and Zelt, 1995). Ray-based traveltime tomography is fast and effective for building velocity models with first arrivals including direct waves and refracted waves. However, ray theory is based on the high-frequency assumption (Aki et al., 1977; Humphreys et al., 1984; Zelt and Barton, 1998; Fu and Hanafy, 2017). As a result, the ray-based traveltime tomography methods require that the velocity is smoother than the scale of the wavelength, the phase delay has a linear relationship with frequency, and the wavelet is not distorted.

To overcome the high-frequency approximation of ray theory, a few finite-frequency-based methods have been proposed, for example, wave equation traveltime (WT) inversion (Luo and Schuster, 1990, 1991; Sieminski et al., 2004), wave equation tomography (Woodward, 1992), and wave path eikonal traveltime inversion (Schuster and Quintus-Bosz, 1993). Luo and Schuster (1990, 1991) propose a form of WT inversion, which can produce more accurate results than ray-tracing traveltime tomography. This method uses crosscorrelation to obtain the traveltime difference between the observed and predicted data. The accuracy of crosscorrelation is directly related to the fidelity of waveforms, so a relatively high S/N record and a good estimation of the wavelet may be needed when applying this WT method to land field data (Sheng et al., 2006). Woodward (1992) integrates the monochromatic wavefield along the wave propagation path. They use the Born and Rytov approximations and demonstrate the band-limited raypath (fat ray) nature. Schuster and Quintus-Bosz (1993) present a general formula for the back projection of traveltime residuals in traveltime tomography and use the eikonal function to calculate the seismic traveltime. Compared with the WT method, the method of Schuster and Quintus-Bosz (1993) is more efficient. Spetzler and Snieder (2004) show that the traveltime is not only influenced by velocity anomalies on the central raypath but also affected by velocities within the first Fresnel zone. Pyun et al. (2005) use the damped monochromatic wavefield to overcome the limitations of the high-frequency assumption of the classical ray method, which could recover smooth velocity models with large offset data. The Gaussian beam method can mitigate the shadow and caustics issue existing in high-frequency ray methods (Červený et al., 1982; Hill, 2001; Cai et al., 2017). Thus, Liu et al. (2014) place Gaussian beams on the Born wave path to simulate the waveform of first arrivals, which decreases the computational cost of FWI significantly.

Because FWI usually uses full wave equations to simulate wavefields, it is not affected by the high-frequency approximation. However, it is still challenging to directly apply FWI on land seismic data due to near-surface complexity and elastic effects in land seismic data. To mitigate the elastic effects of marine seismic data in FWI, several strategies have been proposed. Chapman et al. (2010) and Hobro et al. (2014) add a correction term to the acoustic wave equation with a small extra calculation to compensate for elastic effects in acoustic simulation on the P-wave amplitude. Alternatively, Agudo et al. (2018) develop a matching filtering algorithm to transform elastic data into acoustic data before inversion with acoustic FWI. Yao et al. (2020b) further use supervised deep neural networks to eliminate elastic effects from the field data and then invert the processed data with acoustic FWI. However, strong heterogeneity and softness of near-surface layers cause serious distortion and attenuation to waveforms of land seismic data. These complications impose great challenges for current wavefield modeling tools to accurately simulate the waveforms of land field data. Thus, it is difficult to perform conventional FWI on land data even with these elastic compensation measures.

A smooth background velocity model is adequate for seismic migration. Therefore, it is sensible to recover such a P-wave velocity model for subsequent seismic data migration. Because almost all of the first arrivals are dominated by P waves, which are not interfered by S wave and surface wave signals, we consider using acoustic FWI to invert the first arrivals of land seismic data for recovering the background P-wave velocity.

Surface topography must be considered for land seismic data modeling and inversion. When the earth model is discretized with rectangular grids, the irregular surface will be truncated to the nearest integer points to form a staircase-like surface, which produces artificial diffractions at the edges of staircases during wavefield propagation as well as traveltime errors in surface-related events (Lombard and Piraux, 2004). The artificial diffractions and the traveltime errors also can produce large errors in FWI (Bleibinhaus and Rondenay, 2009). Consequently, successful FWI applications, especially for land seismic data, require efficient and accurate wavefield modeling algorithms to deal with irregular surface topography. To apply the first-arrival waveform inversion (WI) method to land field data, we use an improved immersed boundary method, which can handle irregular surface topography and remains stable during the finite-difference modeling process (Li et al., 2020). The key step of this method is to compute the wavefield at ghost points using the wavefield below the free surface. Li et al. (2020) achieve this goal with an iterative symmetric interpolation.

We aim to recover the P-wave velocity with first-arrival signals of land data, which are dominated by P-wave energy. Consequently, it is reasonable to use an acoustic wave equation with the improved immersed boundary method to accurately simulate the traveltime of the first arrivals. However, the waveforms of real data may not be simulated accurately in this way. In addition, the time difference between the observed data and the corresponding predicted data can be more than half a period, which results in cycle skipping and causes FWI to converge to a local minimum (van Leeuwen and Mulder, 2010; Luo and Sava, 2011; Hu, 2014; Wu et al., 2014; Warner and Guasch, 2016; Liu and Zhang, 2017; Yang and Engquist, 2017; Yong et al., 2019; Chen et al., 2020; Liu et al., 2020; Song and Alkhalifah, 2020). To overcome these two issues, we invert a synthesized intermediate data set containing first arrivals that have been presumably adjusted to remove cycle skipping, which contain the traveltime information of the observed data and are compatible with the acoustic wave equation (Yao et al., 2019). First, we pick the first breaks of the observed data and the predicted data. Then, we shift the first arrivals of the predicted data toward that of the observed data to within half a cycle to decrease the time difference. These shifted data are the intermediate data. Finally, we invert the intermediate data using the WI engine to recover velocity. The applications on land field data sets demonstrates the high effectiveness of this presented method and strategies.

METHOD

Forward modeling with an irregular free surface

The acoustic wave equation can be expressed as

$$\frac{1}{V(\mathbf{x})^2}\frac{\partial^2 p(\mathbf{x},t)}{\partial t^2}-\rho(\mathbf{x})\nabla\cdot\frac{1}{\rho(\mathbf{x})}\nabla p(\mathbf{x},t)=\delta(\mathbf{x}-\mathbf{x}_s)s(t), \quad (1)$$

where $p(\mathbf{x}, t)$ represents the pressure field, V indicates the velocity, ρ represents the density, $s(t)$ denotes the source signature, and $\delta(\mathbf{x} - \mathbf{x}_s)$ represents the Dirichlet delta function for injecting the source at the source location $\mathbf{x}_s$.

When we perform numerical simulations of the seismic wavefield using the finite-difference method, conventional rectangular grids are common choices. However, if the free surface in the irregular topography land case is discretized with rectangular grids, the true earth's surface will be truncated to the nearest integer points and will form a staircase-like surface, which generates artificial diffractions at the edges of the staircases as well as traveltime errors (Lombard and Piraux, 2004). In this paper, we use the immersed boundary method with an iterative symmetric interpolation to handle this problem (Li et al., 2020). This method can be summarized as follows.

1) We first add ghost points (Figure 1) at each location above the irregular free boundary and set the number of grid points to be one-half the length of the spatial finite-difference stencil to perform a finite-difference operation for each grid point below the surface.
2) For each ghost grid point, we determine its mirror point by assuming the surface as a plane of symmetry (Figure 1).
3) For each time step, we first set the wavefield at all the ghost grid points to be zero and compute the wavefield below the surface using the regular finite-difference scheme. Once the wavefield is obtained, we use a 2D Kaiser-windowed Sinc interpolation to compute the wavefield at the mirror points. We then set the wavefield at the ghost points to the negative of the values of their corresponding mirror points.
4) We continue to repeat step (3) until the ghost wavefield becomes stable.

In these steps, because the position of the mirror points only needs to be searched once in the whole modeling process, the increased computation mainly comes from the iterative interpolation. Our test shows the process of interpolation converges in no more than 20 iterations. In addition, the interpolation performs only on the grid points near the surface. As a result, the increased computation is much less than the finite-difference operation. Furthermore, the entire modeling process is significantly faster than using finer grids. Readers are referred to Li et al. (2020) for more details about the immersed boundary method used in this paper.

FWI for land seismic data

FWI aims to find a suitable subsurface model that minimizes the differences between the observed records and the predicted records. The objective function of FWI can be chosen as

$$f(\mathbf{m}) = \frac{1}{2}\|\mathbf{d}_{\text{cal}} - \mathbf{d}_{\text{obs}}\|_2^2, \tag{2}$$

where $\mathbf{m}$ represents the model parameters and $\mathbf{d}_{\text{cal}}$ and $\mathbf{d}_{\text{obs}}$ denote the predicted data and the observed data, respectively (Tarantola, 1984; Pratt, 1999; Sears et al., 2008; Virieux and Operto, 2009). By minimizing the objective function $f(\mathbf{m})$, the corresponding model $\mathbf{m}$ is the result of FWI.

In general, local gradient methods are used to update the model. With the steepest-descent method, the update $\Delta\mathbf{m}$ can be approximated as

$$\Delta\mathbf{m} = -\alpha\nabla_{\mathbf{m}} f = -\alpha\left(\frac{\partial\mathbf{d}_{\text{cal}}}{\partial\mathbf{m}}\right)^{\dagger}(\mathbf{d}_{\text{cal}} - \mathbf{d}_{\text{obs}}), \tag{3}$$

where α is the optimal step length and $\nabla_{\mathbf{m}} f$ is the gradient of the objective function with respect to the model parameters. The adjoint state method is generally used to calculate the gradient of the objective function without forming the Jacobian matrix, $\partial\mathbf{d}_{\text{cal}}/\partial\mathbf{m}$, explicitly. The acoustic wave equation 1 can be discretized as a linear equation system in a matrix-vector form:

$$\mathbf{A}\mathbf{u} = \mathbf{s}, \tag{4}$$

where $\mathbf{A}$ represents the wave equation operator and $\mathbf{u}$ denotes the seismic wavefield from the source function $\mathbf{s}$. The gradient of FWI then can be expressed as follows:

$$\nabla_{\mathbf{m}} f = -\bar{\mathbf{u}}^T\left(\frac{\partial\mathbf{A}}{\partial\mathbf{m}}\right)^T\bar{\bar{\mathbf{u}}}, \tag{5}$$

where $\bar{\mathbf{u}}$ denotes the forward-propagated source wavefield by solving equation 4 and $\bar{\bar{\mathbf{u}}}$ represents the backward-propagated residual wavefield at every receiver by solving

$$\mathbf{A}^T\bar{\bar{\mathbf{u}}} = \mathbf{d}_{\text{cal}} - \mathbf{d}_{\text{obs}}, \tag{6}$$

where $\mathbf{A}^T$ is the adjoint operator of $\mathbf{A}$. Because $\mathbf{A}$ is self-adjoint for the isotropic acoustic wave equation 1, $\mathbf{A}^T$ is equal to $\mathbf{A}$. To compute $\bar{\bar{\mathbf{u}}}$, we only need to backward propagate the adjoint source, $\mathbf{d}_{\text{cal}} - \mathbf{d}_{\text{obs}}$. As a result, the calculation of the gradient in each iteration requires two wavefield simulations (one for source forward propagation modeling and another for residual backward propagation modeling).

In a land field seismic survey, the receivers are geophones that are placed on (or slightly below) the free surface to record the particle

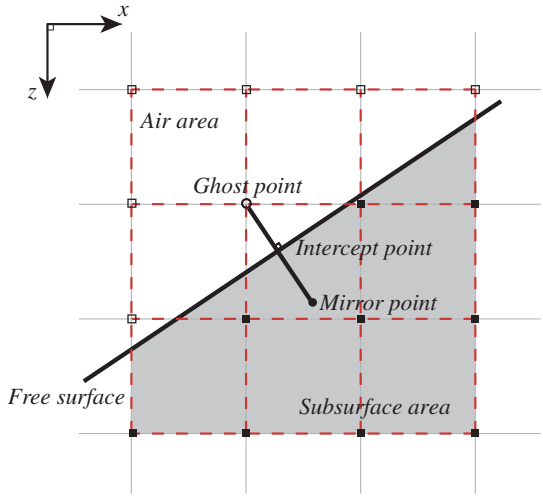

Figure 1. Schematic diagram of the immersed boundary method in the 2D space domain. The solid black line represents the irregular free surface boundary. The gray area represents the subsurface area, whereas the white area represents the air area above the surface boundary. The unfilled circle represents a ghost point on an integer node above the free surface boundary, whereas the filled circle indicates its mirror point on a fractional node below the boundary. The straight line across a pair of the mirror and ghost points is orthogonal to the free surface, and the vertical foot is the intercept point.

velocity (usually the vertical component v_z). To form the gradient of the objective function with particle velocity, we can transform equation 1 into the first-order acoustic wave equation system,

$$\begin{cases} \frac{\partial v_x}{\partial t} = \frac{1}{\rho}\frac{\partial p}{\partial x} \\ \frac{\partial v_z}{\partial t} = \frac{1}{\rho}\frac{\partial p}{\partial z} \\ \frac{\partial p}{\partial t} = K\left(\frac{\partial v_x}{\partial x} + \frac{\partial v_z}{\partial z}\right) \end{cases}, \tag{7}$$

where v_x and v_z are the particle velocity in the horizontal and vertical directions, respectively, and K is the bulk modulus which is equal to ρv^2. The first-order acoustic wave equations can be discretized into a matrix-vector form similar to equation 4, in which the wave equation operator $\mathbf{A}$ and the seismic wavefield $\mathbf{u}$ will be expressed as follows:

$$\mathbf{A} = \begin{bmatrix} \rho\frac{\partial}{\partial t} & 0 & -\frac{\partial}{\partial x} \\ 0 & \rho\frac{\partial}{\partial t} & -\frac{\partial}{\partial z} \\ -\frac{\partial}{\partial x} & -\frac{\partial}{\partial z} & \frac{1}{K}\frac{\partial}{\partial t} \end{bmatrix} \tag{8}$$

and

$$\mathbf{u} = \begin{bmatrix} v_x \\ v_z \\ p \end{bmatrix}. \tag{9}$$

As a result, the derivative of $\mathbf{A}$ with respect to the bulk modulus K at a certain spatial point and at a certain time can be expressed as

$$\frac{\partial \mathbf{A}}{\partial K} = \begin{bmatrix} 0 & 0 & 0 \\ 0 & 0 & 0 \\ 0 & 0 & -\frac{1}{K^2}\frac{\partial}{\partial t} \end{bmatrix}. \tag{10}$$

The gradient of the objective function with respect to the bulk modulus then is expressed as follows:

$$\nabla_K f = -\begin{bmatrix} \vec{v}_x \\ \vec{v}_z \\ \vec{p} \end{bmatrix}^T \begin{bmatrix} 0 & 0 & 0 \\ 0 & 0 & 0 \\ 0 & 0 & -\frac{1}{K^2}\frac{\partial}{\partial t} \end{bmatrix} \begin{bmatrix} \overleftarrow{v}_x \\ \overleftarrow{v}_z \\ \overleftarrow{p} \end{bmatrix}, \tag{11}$$

where "$\rightarrow$" represents the forward propagation and "$\leftarrow$" represents the backward propagation. Finally, the gradient of the objective function with respect to bulk modulus is

$$\nabla_K f = \frac{\partial f}{\partial K} = \frac{1}{K^2}\frac{\partial \vec{p}}{\partial t}\overleftarrow{p}. \tag{12}$$

By using the chain rule, the gradient of the objective function with respect to the P-wave velocity is as follows:

$$\frac{\partial f}{\partial V} = 2\rho V\frac{\partial f}{\partial K} = \frac{2}{\rho V^3}\frac{\partial \vec{p}}{\partial t}\overleftarrow{p}. \tag{13}$$

As can be seen from equation 13, the gradient of velocity depends only on the pressure component. Therefore, we solve equation 1 instead of equation 7 to reduce computational cost. During the forward modeling, we solve equation 1 first and then apply equation 7 to calculate v_z only at the receiver location. During the backward propagation step, we simplify the adjoint equation 6 for the first-order equation 7 to

$$\frac{1}{V(\mathbf{x})^2}\frac{\partial^2 \overleftarrow{p}(\mathbf{x},t)}{\partial t^2} - \rho(\mathbf{x})\nabla\cdot\frac{1}{\rho(\mathbf{x})}\nabla\overleftarrow{p}(\mathbf{x},t) = \delta(\mathbf{x}-\mathbf{x}_r)\frac{\partial \delta v_z(\mathbf{x}_r,t)}{\partial z}, \tag{14}$$

where δv_z represents the adjoint source, i.e., the data residual of the vertical component of particle velocity in the objective function in equation 2, and $\mathbf{x}_r$ indicates the receiver location. Note that the gradient in equation 13 has a first-order time derivative instead of a second-order time derivative used usually for inverting pressure data. This can be explained in equation 14: its spatial derivative in the adjoint source plus the time derivative in the gradient acts as a second-order derivative.

WI with the first arrivals

If we apply the objective function in equation 2 to invert the first arrivals of land seismic data, we usually face two challenges: first, the cycle-skipping problem; second, inconsistent waveforms between the predicted data and observed data due to noise, elasticity, and other factors. To recover the P-wave velocity robustly, we invert intermediate data, the first-arrival events that are created by shifting the first arrivals of the predicted data toward the corresponding events of the observed data within half a cycle (Yao et al., 2019). We then implement the first-arrival WI based on the following steps:

1) Pick the first breaks of the observed data (Wong et al., 2009).
2) Generate predicted data and pick the first breaks of the predicted data.
3) Calculate the traveltime difference of first arrivals between the observed data and the predicted data, and smooth the calculated time differences to remove any outliers.
4) Generate the intermediate data by shifting the predicted data toward the observed data with the time shifts that are less than half a cycle.
5) Produce a Gaussian window function to select the first-arrival wave parts of intermediate data for WI. The length of the selected time window can be adjusted based on the synthetic data to include the first-arrival signals.
6) Update velocity model by using WI.
7) Return to step (2) until convergence.

The algorithm depicted previously shifts the predicted data multiple times by less than half a period both to avoid cycle skipping as well as to compensate for waveform inconsistencies. Theoretically, this method only needs the first-arrival time curve of each shot record to perform inversion; therefore, it is robust in real data applications.

EXAMPLES

We first use the Canadian foothills synthetic model to verify the proposed method. We then apply the WI method to three land field data sets to demonstrate its effectiveness for field data.

Synthetic example: The Canadian foothills model

The Canadian foothills model is a 2D synthetic model (Figure 2a) that captures the common geologic features of the Canadian foothills in northeastern British Columbia (Gray and Marfurt, 1995). We have selected it as our synthetic test model partly because of its rugged topography to demonstrate that our WI method can handle topography well due to the use of the immersed boundary method. We also want to verify that using the proposed acoustic wave-based inversion scheme can recover the P-wave velocity structure of the input model. To do so, we have generated two sets of synthetic seismograms: (1) acoustic synthetics and (2) full elastic synthetics. One shot profile is depicted in Figure A-1. The acoustic synthetic data set is generated by solving the acoustic wave equation with the immersed boundary method, whereas the elastic data set is computed by using the SPECFEM2d (Tromp et al., 2008; Komatitsch et al., 2010) package. We set $V_S = 0.6V_P$ in the elastic wavefield simulation. Each synthetic data set consists of 82 shots fired at the first integer cell below the free surface. The receiver array includes 1668 receivers uniformly spaced placed on the entire surface to record the vertical component of particle velocity only. The source wavelet is a 15 Hz Ricker wavelet, and the time sampling interval is 0.5 ms.

Then, we apply this proposed WI scheme to the two data sets. We first smooth the input model (Figure 2a) to create an initial velocity model (Figure 2b) for the WI process. The inverted velocity models using the acoustic and elastic synthetic data sets are shown in Figure 2c and 2d, respectively. The two inverted models are very similar to each other, and both effectively recover the near-surface velocity structure of the input model, suggesting that the proposed acoustic-based WI method can invert full elastic data as long as only the first arrivals are used.

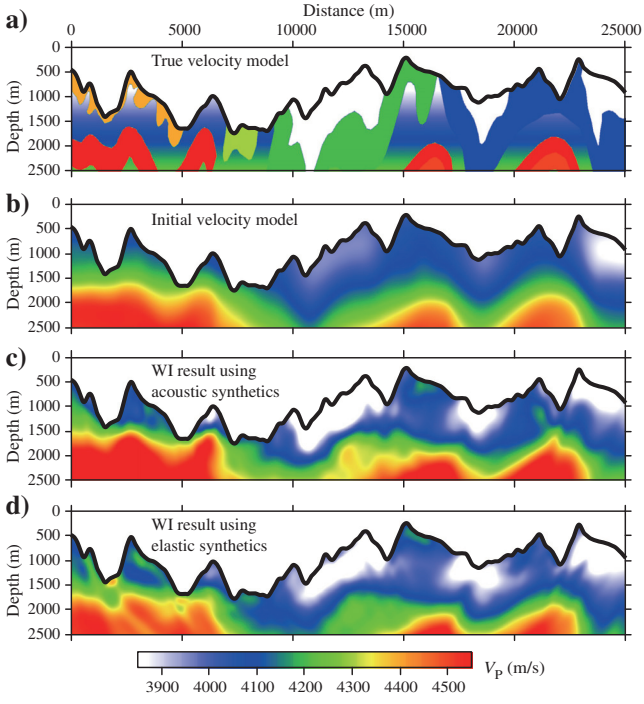

Figure 2. The top part of the input and output P-wave velocity structures of the Canadian foothills model. (a) The true velocity model. (b) The initial velocity model for WI. (c and d) The WI inversion results by inverting the synthetic seismograms generated by the acoustic and elastic wave equations, respectively.

Land data example 1

The surface elevation of the study area is shown by the black curve in Figure 3. This data set includes a total of 38 shots generated with dynamite. Each shot has 72 receivers with an interval of 10 m and a maximum offset of 360 m. The shot spacing is 60 m. This survey aims to investigate the near-surface geologic structure. Due to the low S/N of the original shot gathers, the first-arrival curves are picked manually. Ray-based traveltime tomography and WI with first arrivals are carried out. During the inversion process, the near offsets and severely low S/N regions are excluded from the inversion.

The inversion starts from a 1D initial velocity model with linearly increasing velocity from shallow to deep, which is shown in Figure 3a. We have used a commercial software package (ToModel) to perform the traveltime tomography. The 2D velocity model and the ray density are shown in Figure 3b and 3c, respectively. It is worth noting that the ray-based tomography inversion itself updated the model effectively only in the region covered by the seismic rays (above the dashed blue line). Below this region, velocity is obtained by extrapolation. Therefore, the reliability of the inverted model in the ray-covered area is higher than in the other area. As can be seen, the rays only cover the model to a depth of 180 m, which indicates the reliable depth of ray-based inversion. In general, the higher the ray density, the more reliable the inversion result.

Then, we carried out WI with the v_z component, which is the component recorded on the free surface. As the S/N is low at

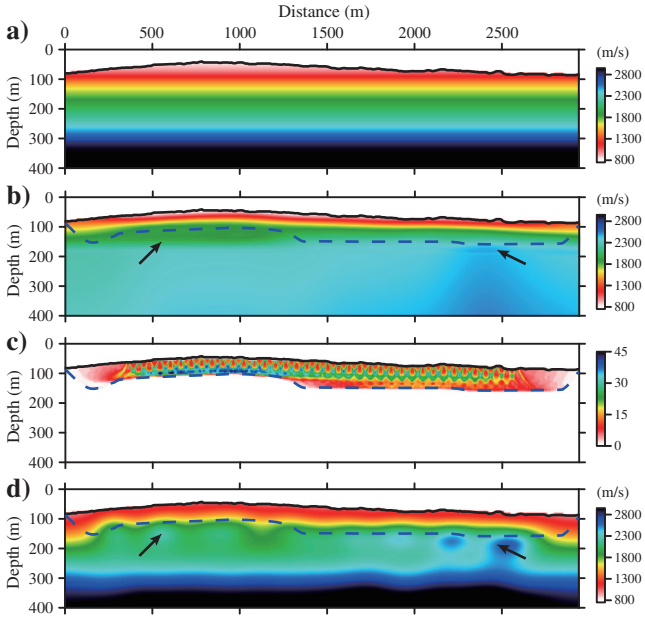

Figure 3. Results of inversion. (a) The 1D initial velocity model for tomography and WI. (b) Recovered velocity model with ray-based traveltime tomography. (c) Ray density map. The color indicates the number of rays that cross this cell. (d) The inverted velocity model using WI with first arrivals. The dashed blue curves indicate the ray coverage, which is within 180 m in depth. The black arrows point to the resolution difference in the two inversion results. Note that there is a strong acquisition footprint in the density map in (c), which is less obvious in the inverted model shown in (d).

DOI:10.1190/geo2021-0097.1

the near-offset parts and the amplitude of land seismic data is not very reliable, we did not extract the source wavelet from seismic data for inversion but used a 30 Hz Ricker as the source wavelet for inversion. Offsets less than 100 m were excluded in the inversion because the low S/N at the near offsets prevents reliable first-arrival picking. The inversion process started from 2 Hz up to 30 Hz for 55 iterations in total.

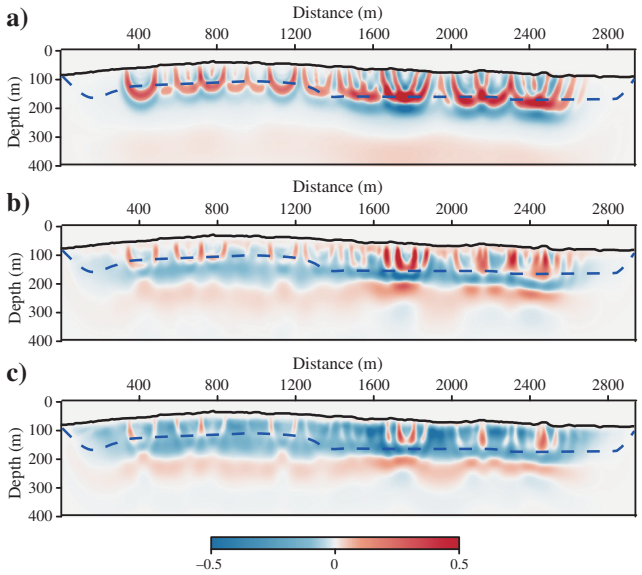

Figure 4. The gradients in the inversion process of WI. (a–c) The normalized gradient for the 1st, 11th, and 16th iterations, respectively. The dashed blue curves indicate the ray coverage boundary.

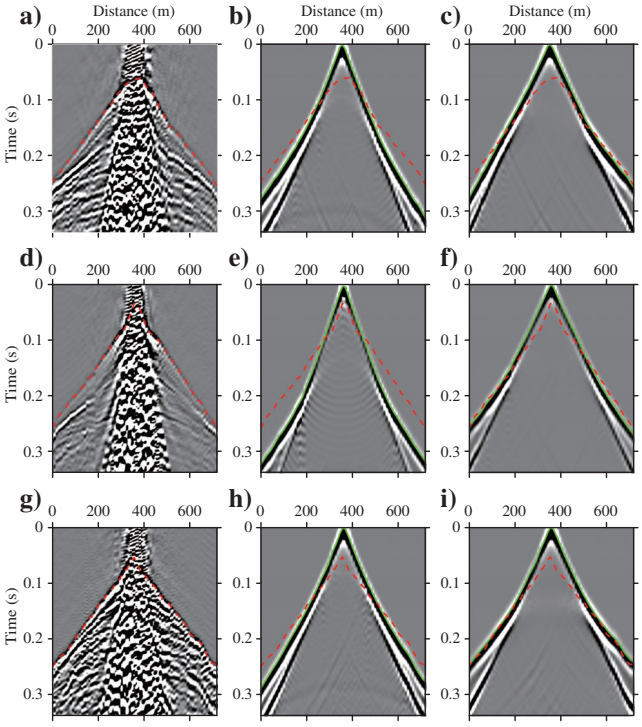

Figure 5. Seismic gathers of three shots. (a, d, and g) The first column shows the observed land field data, whereas (b, e, and h) the second column and (c, f, and i) the third column depict the corresponding predicted record generated from the initial model and the final inverted model, respectively. The dashed red curves represent the picks of the first arrivals of observed data, whereas the green curves are for the predicted data.

The final recovered velocity model is shown in Figure 3d. By comparison, it is obvious that WI recovered some high-velocity anomalies, which are indicated by the black arrows, more clearly than the ray-based traveltime tomography. In addition, the model update depth of the inversion is greater because WI updates the cells of the model covered by the first Fresnel zone, which is much wider than rays. This is confirmed by the normalized gradients shown in Figure 4.

The inversion quality also is confirmed by the good match of the first-arrival picks between the observed data and the predicted data from the inverted model (Figure 5). We deliberately show some mismatch on the left side of the first shot (Figure 5c) because there is no other shot on the left side of the first shot, resulting in inadequate updates.

Figure 6 shows the histograms that indicate the first-arrival traveltime errors of the initial model and the inverted velocity model at different iterations. As the number of iterations increases, the traveltime errors decrease gradually and the bars of the histograms are more concentrated around zero. Note that the mean value of WI also is smaller than that of the ray-based tomography.

Land data example 2

To further verify the effectiveness of the proposed method, we have performed the inversion on another land data set acquired in Western China. The survey is in the transition zone between the Tianshan Mountains and the Tarim Basin. It has complex surface topography and geologic structures, which poses a great

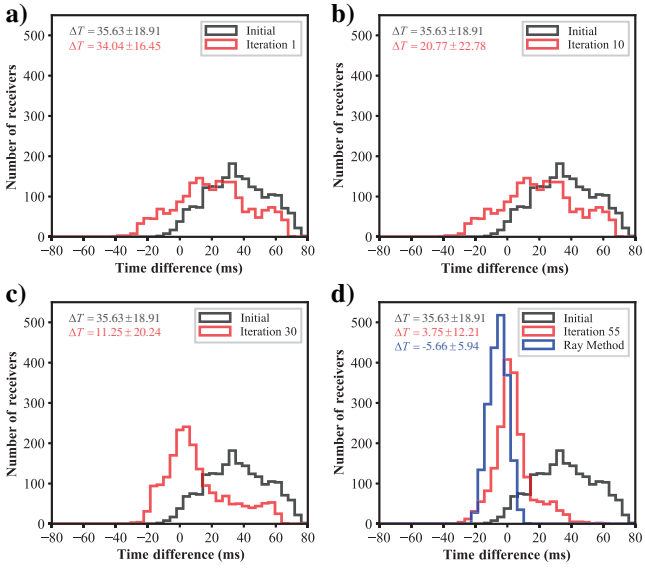

Figure 6. The histogram of the first-arrival traveltime difference between the predicted data and the observed data. (a–d) The histograms for the 1st, 10th, 30th, and 55th iterations in the WI process, respectively. The gray and red lines indicate the traveltime difference calculated using the initial model and the WI inverted models, respectively. The blue line in (d) indicates the traveltime difference calculated using the ray-based tomography method; ΔT indicates the mean values plus/minus the standard deviations.

challenge for reflection-based velocity building methods, including reflection-based traveltime tomography. This data set has a total of 242 shots with a maximum offset of 7200 m, which is much larger than that of the first data set. Dynamite has been used as the source in this survey. Figure 7 shows three typical raw shot gathers in the study area. They show a typical problem of applying FWI or other velocity building methods on land seismic data: low S/N. In this data set, the apparent S/N does not allow reflection events to be directly visible. As shown in Figure 7, it is even difficult to pick the first arrival in some areas. In this case, the conventional FWI method struggles to find an acceptable model and a wavelet to match the waveforms in the records, even the first arrivals. This also is the reason why we have only used the time information of first arrivals for inversion.

Due to the obvious irregular topography in this study area, we have found that accurate forward modeling with proper treatment of the surface topography becomes important. In this study, we have used an improved immersed boundary method (Li et al., 2020) for simulating the surface topography. As a comparison, we also have tested the vacuum method, which is commonly used but less effective. Figure 8 shows a shot gather computed with the conventional vacuum method (Graves,1996) and the immersed boundary method. The vacuum method forces the free surface to its nearest integer grid locations, resulting in a staircase-like artificial boundary that generates strong diffractions from the stair corners (Figure 8a). In addition, truncating the free surface to its nearest integer grid points also leads to noticeable discrepancies in the first-arrival time (Figure 8c and 8d). This could introduce errors in the inverted model.

The initial model is shown in Figure 9a, which is a modified 1D velocity model with velocity isolines being parallel to the surface topography. The inversion result from ray-based tomography is shown in Figure 9c. The model evolution is shown in Figure A-2. Ray density is shown in Figure 9d. As shown in Figure 9d, obvious shadow and caustics areas exist when using ray-based methods, which are pointed out by the black and red arrows, respectively. The ray shadow leads to insufficient updates, whereas the ray caustics result in erroneously large updates. In these areas, the velocity obtained using ray-based tomography is not reliable.

The shadow and caustics problems can be avoided by using our WI method. A Ricker wavelet with a dominant frequency of 15 Hz has been selected as the source wavelet in the inversion process. The

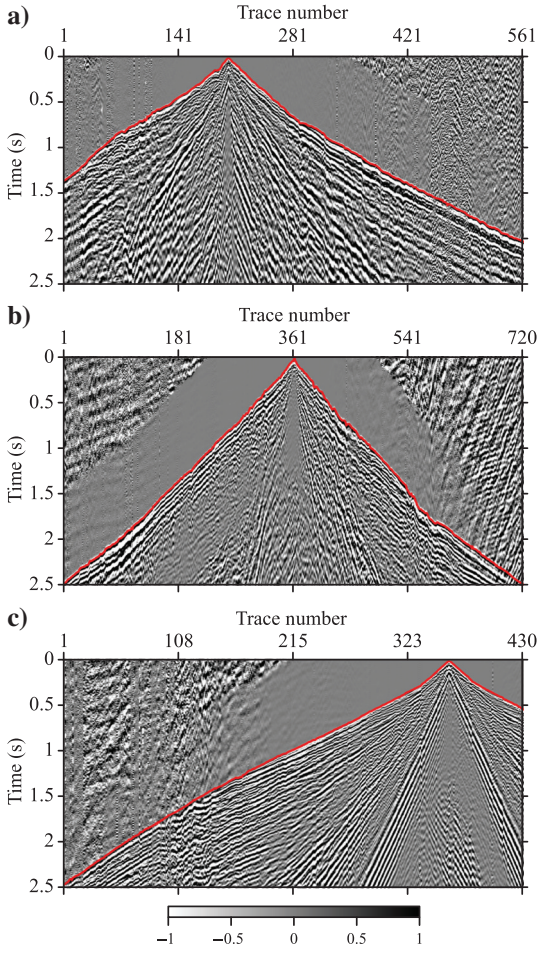

Figure 7. Three typical shot gathers in the study area. The red curves indicate the first arrivals.

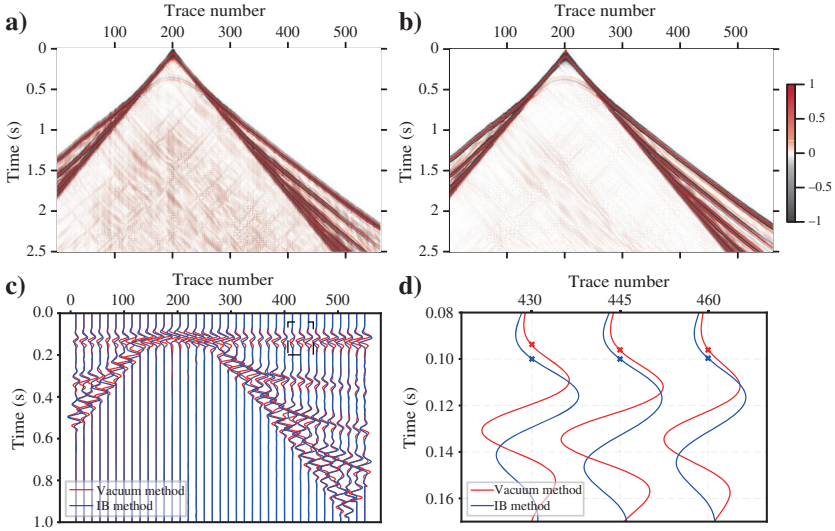

Figure 8. The synthetic shot gathers from the initial model shown in Figure 9a. (a and b) The shot gathers with the vacuum method and the immersed boundary method, respectively. (c) The wiggle display of the shot gathers in (a) and (b) after a moveout correction based on the first-arrival times and (d) the magnified display of the black box area of (c). The red and blue crosses "×" indicate the first-arrival picks of each trace from the vacuum method and IB method, respectively.

inversion process includes 70 iterations starting from 2 Hz up to 15 Hz. We also use the 1D velocity model as the starting model for the WI. The inverted model is shown in Figure 9e. The model evolution is shown in Figure A-3. For comparison, we also have conducted a similar WI using the conventional vacuum method as the forward-modeling engine, and the result is shown in Figure 9f. The two models derived from WI (Figure 9e and 9f) generally show similar velocity structures. The minor difference between the two WI models is caused by the inaccuracy of the vacuum method. However, both WI models possess improved resolution as compared with the ray-based traveltime tomography model. The deeper penetration of WI can be observed from the normalized gradients shown in Figure 10. The gradients also demonstrate that WI is immune to the shadow and caustics problem.

Figure 11 shows the evolution of the first-break picks of the three shots in Figure 7. As the number of iterations increases, the first breaks of the predicted data are closer to those of the observed data. This means WI improves the data fit successfully.

Figure 12 shows the histograms that depict the first-arrival traveltime residuals of the initial model and the inverted velocity models at different iterations. Compared with the previous example, more shots and traces are involved in the inversion. As a result, the traveltime errors converge very well for WI with our immersed boundary method and the ray-based tomography. However, the result of WI with the vacuum method at each iteration has larger traveltime errors, which implies that the recovered velocity model with the

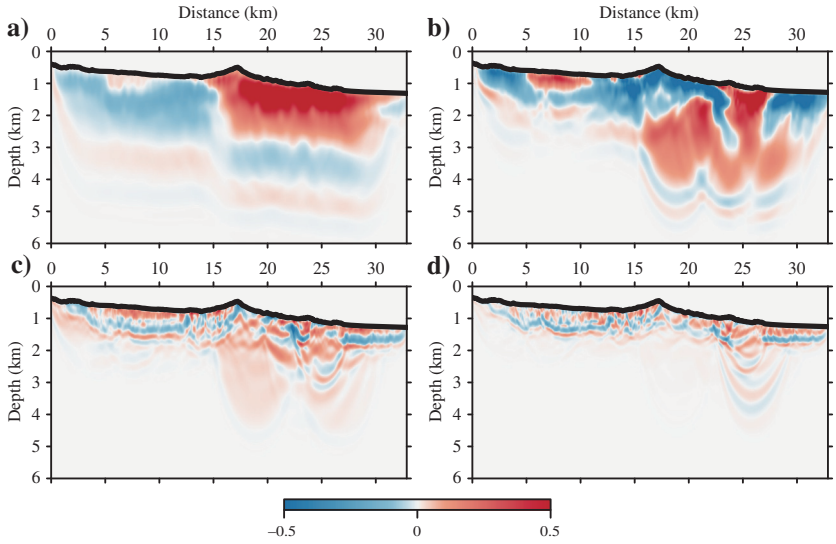

Figure 10. The gradients of WI. (a–d) The normalized gradient for the 1st, 20th, 40th, and 70th iterations, respectively.

Figure 9. The velocity profiles and ray density map for the second land field survey. (a) The 1D initial velocity model for inversion. (b) The surface elevation for the study area. (c) Recovered velocity profile using ray-based tomography. (d) Ray density map. (e) Recovered velocity profile using WI with first arrivals based on the immersed boundary modeling method. (f) Recovered velocity profile using WI with first arrivals based on the vacuum modeling method. The black lines indicate the surface topography and the dashed blue lines represent the coverage of rays. The black and red arrows point to the shadow and caustics areas that exist in the ray-based method, respectively.

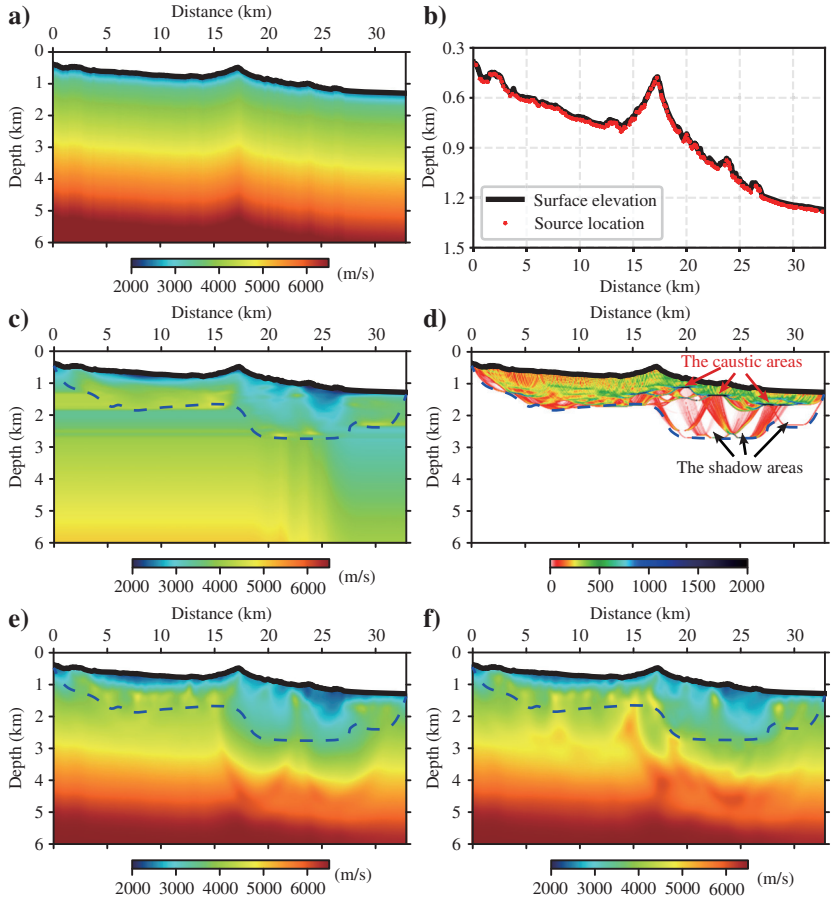

vacuum method (Figure 9f) has larger errors than that with our immersed boundary method. Thus, we infer that the immersed boundary method is a better modeling engine than the vacuum method for land data inversion with irregular surface topography. Further comparison has found that the mean value of traveltime difference calculated by our method at the 70th iteration is still smaller than the ray-based tomography. Thus, this example demonstrates that our WI method can ensure the reliability of the inversion process of velocity building while maintaining better inversion depth and resolution.

Land data example 3

To further illustrate the effectiveness of our inversion method for land field data, we have selected another survey with better data quality, where reflection events can be observed even in the raw data set. After inversion, we perform prestack depth migration (PSDM) to evaluate the accuracy of the inverted velocity.

The third field survey includes 234 shots generated by dynamite. The surface of the study area is relatively flat, where the elevation variation is within 100 m. The maximum offset of all shots is 4200 m. We manually pick the first arrivals of the observed data set. Figure 13 shows two typical shot gathers in the study area.

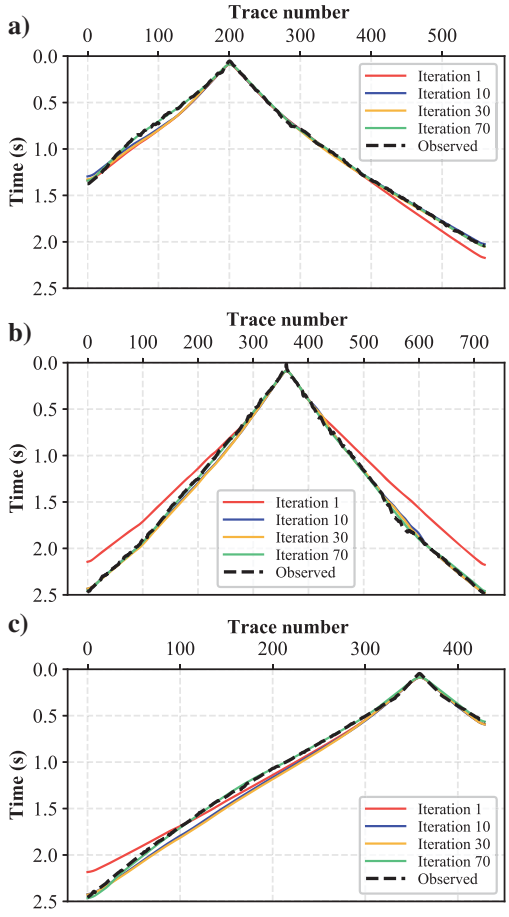

Figure 11. (a–c) Evolution of first breaks throughout the iterations for the three shots shown in Figure 7a–7c, respectively. The dashed black line indicates the first breaks of the observed data, whereas the color lines indicate the first breaks at different iterations.

Due to the relatively high S/N of the data, we extract the source wavelet from the observed seismic data by stacking the record after a moveout correction. The wavelet and its amplitude spectrum are

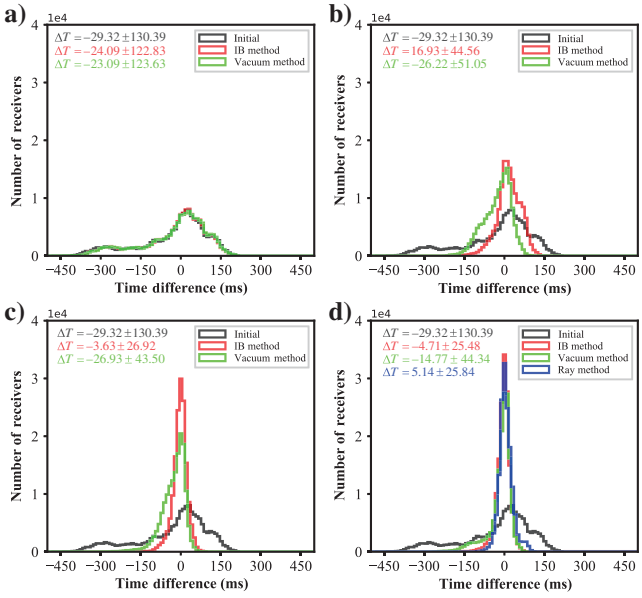

Figure 12. The histogram of the first-arrival traveltime difference between the predicted data and observed data. (a–d) The histograms for the 1st, 20th, 40th, and 70th iterations, respectively. The gray lines indicate the traveltime difference calculated using the initial model. The green and red lines indicate the traveltime difference calculated using the WI models based on the vacuum method and the immersed boundary method, respectively. The blue line in (d) indicates the traveltime difference calculated from the result of the ray-based tomography method; ΔT indicates the mean values plus/minus the standard deviations.

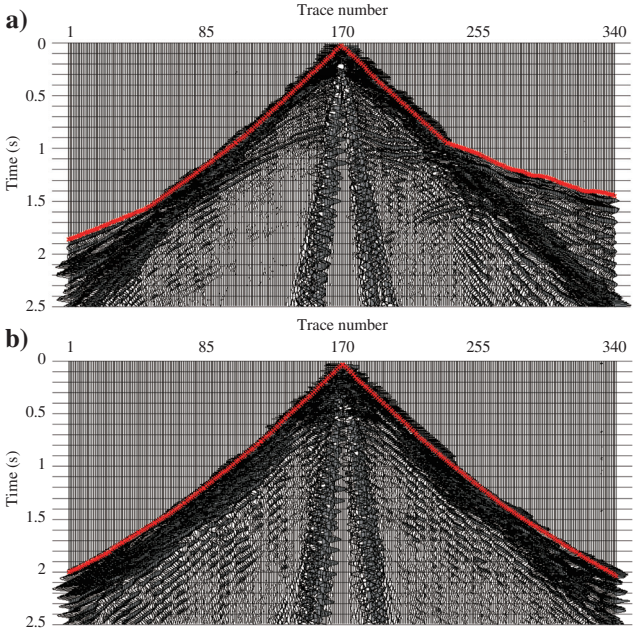

Figure 13. Two typical shot gathers. The red curves indicate the first arrivals.

shown in Figure 14. Then, we use the extracted wavelet as the source wavelet for inversion.

The initial model for the inversion is shown in Figure 15a. Because the area has a very simple structure, a mini basin on top of a buried hill, we have inverted waveform data in a relatively low-frequency band for a total of 70 iterations. The inversion starts from 2 Hz up to 5 Hz with an interval of 1 Hz. The frequency selection is achieved by band-pass filtering. The recovered velocity model from the tomography method is shown in Figure 15c. We have used the initial model and the tomography model as the starting model for our WI. The inverted velocity models are shown in Figure 15e and 15g, respectively. In general, the two WI models inverted from different starting models are relatively similar in the depth range covered by the first arrivals (above the dashed blue line in Figure 15e and 15g). The two models also reveal more details than the tomography model (Figure 15c) on the top boundary of the buried hill in the right part of the profile (indicated by the white arrows in Figure 15e and 15g). The similarity of the two WI models implies that our inversion method is relatively insensitive to the starting model.

To validate the data fit of different models, we further apply Kirchhoff PSDM using the preceding four models as the migration velocity model. The PSDM results are shown in Figure 15b, 15d, 15f, and 15h. As shown in the results, the migration images based on the two WI models generally focus better than those based on the initial model and the tomography model. Specifically, the PSDM images with the two WI models have a clearer and more focused

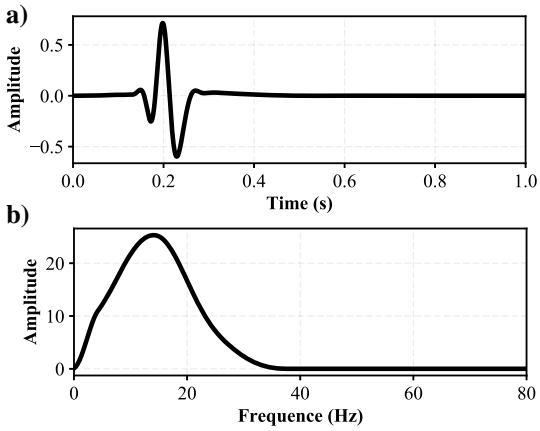

Figure 14. The source wavelet (a) extracted from the observed record and (b) its corresponding amplitude spectrum.

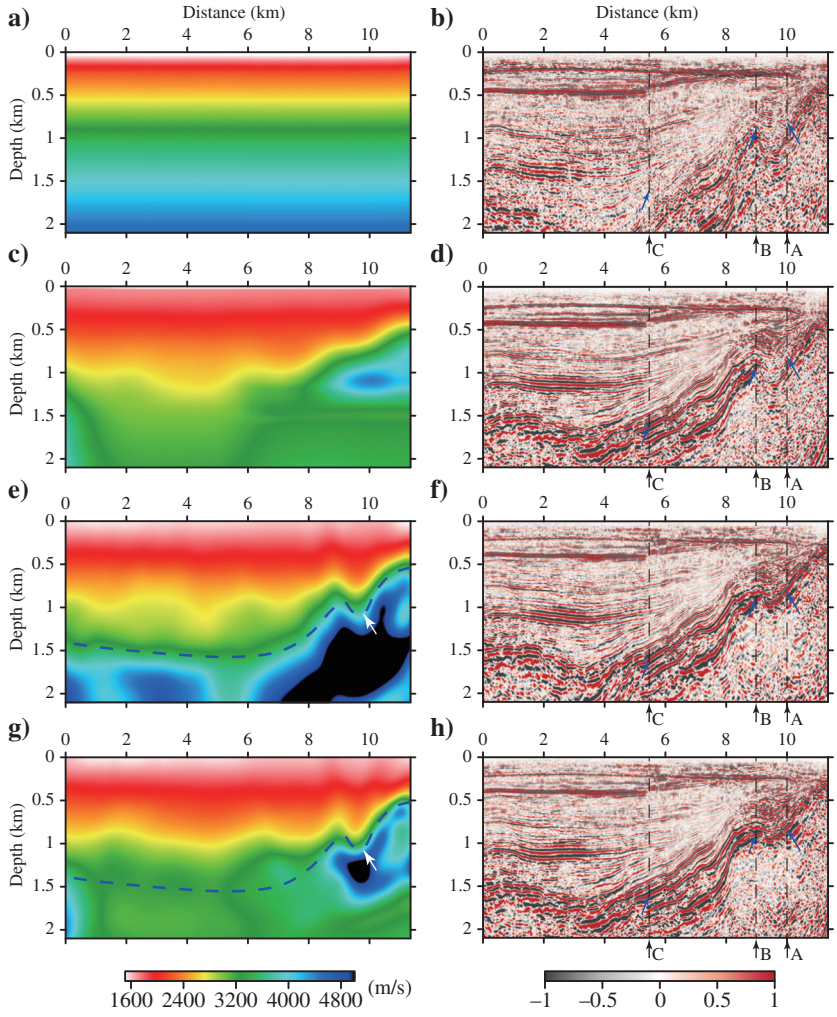

Figure 15. The velocity profiles and the migration image for the third land field survey. (a) The 1D initial velocity model. (c) The inverted velocity models from the ray-based tomography. (e and g) Inverted velocity models with the WI method started from (a) the initial model and (c) the ray-based tomography result. (b, d, f and h) The migration images with Kirchhoff PSDM based on the velocities in (a), (c), (e), and (g), respectively. The black arrows and dashed lines indicate the location of the imaging gathers for comparison, and the blue arrows indicate the events marked by the blue arrows in the corresponding imaging gathers in Figure 16. The dashed blue lines indicate the effective update depth of WI and the white arrows point to the significant difference area compared with the tomography model.

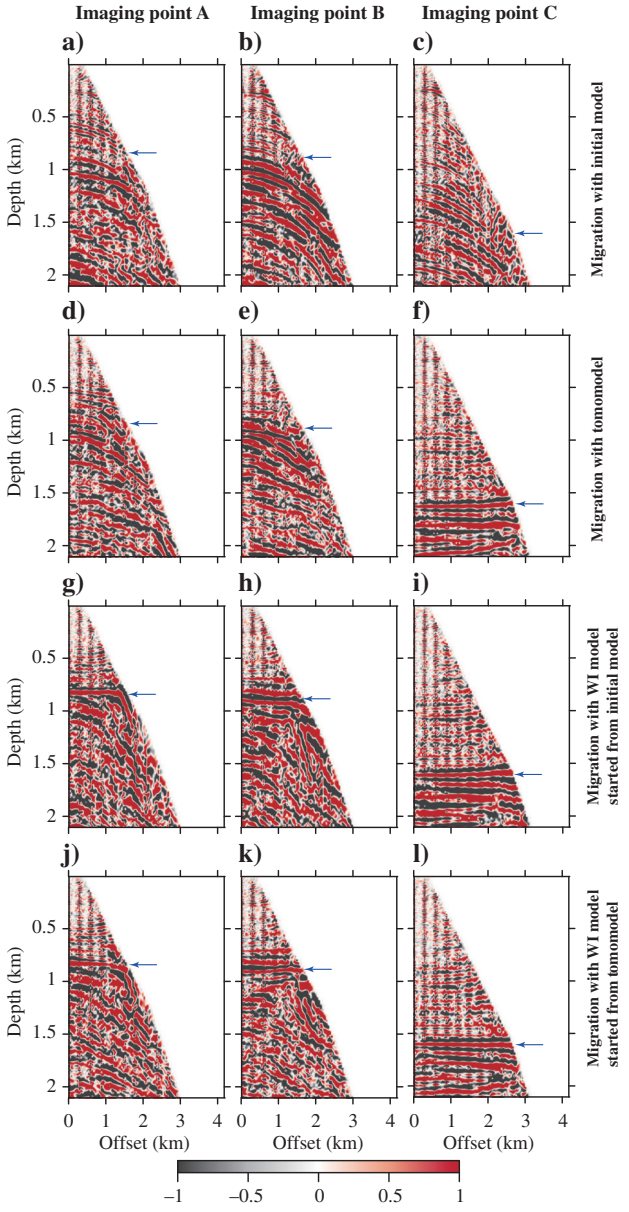

Figure 16. The PSDM gathers for the three models in Figure 15. The three columns from left to right represent the three imaging positions A, B, and C in Figure 15, respectively. The four rows of the CIGs from top to bottom are generated using the velocity models in Figure 15a, 15c, 15e, and 15g, respectively.

top boundary of the buried hill. A further comparison is demonstrated from the common-image gathers (CIGs) shown in Figure 16. It is evident that the events indicated by the blue arrows are flatter in the CIG with WI models than those with the initial model and the tomography model (Figure 16a, 16d, 16g, and 16j and Figure 16b, 16e, 16h, and 16k). In contrast, the events indicated by the blue arrows in the imaging point C (Figure 16c, 16f, 16i, and 16l), where the geology structure is relatively simple, have similar flatness for the tomography model and the two WI models. This suggests that the first-arrival WI has more advantages than the ray-based traveltime tomography in areas with complicated structures.

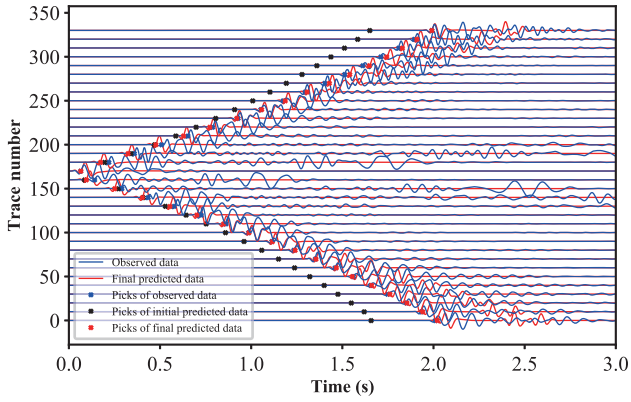

Figure 17. Waveform of one typical shot. The blue and red curves represent the waveforms of the observed data and the final predicted data, respectively. The blue, black, and red crosses "×" indicate the first-arrival picks of each trace for the observed data, initial predicted data, and final predicted data, respectively.

Figure 17 shows the waveform comparison between the final predicted data based on the inverted model in Figure 15g and the observed data. As shown, the waveform of the observed data changes rapidly from one trace to another, whereas it changes much more smoothly for the predicted data. This imposes a significant challenge to waveform-comparison-based FWI for land data. Meanwhile, the traveltime of the first arrivals is much more stable than the waveform for the observed data. Therefore, the traveltime information of the arrivals is reliable for inversion. Consequently, the WI method moves the first-arrival picks of the initial model efficiently to the picks of the observed data.

CONCLUSION

We propose a robust approach that inverts first arrivals of land seismic data. It includes four distinct features. (1) The acoustic wave equation is used for inverting the first arrivals of land seismic data. Unlike the usual practice of recording pressure in the marine environment, the particle velocity, especially its vertical component, is usually recorded in the land data. Thus, the acoustic wave equation simulates the particle velocity field. (2) The velocity field residual is consequently used as the adjoint source for computing the gradient. The formulas of the gradient and the adjoint source are derived to fulfill this purpose. These formulas are different than the counterpart for pressure data, which are normally acquired in the marine environment. (3) An improved immersed boundary method is used for dealing with fluctuated topography more accurately, especially in the case of a coarse grid implementation. The key aspect of the immersed boundary is that the ghost wavefield is computed with an iterative interpolation method. (4) The intermediate data set is created to avoid cycle skipping. The data set is generated by shifting the predicted data toward the observed data within half a cycle. We demonstrate the effectiveness of this proposed algorithm with the Canadian foothills model and three land field data sets. The applications show that the proposed method can recover P-wave velocity models with higher resolution and deeper penetration than ray-based traveltime tomography. These results can be used as a high-quality velocity model for PSDM. This method is particularly valuable for low S/N land data, on which the reflection-based migration velocity analysis methods are ineffective.

ACKNOWLEDGMENTS

This work was partially supported by National Key R&D Program of China (grant nos. 2017YFC1500303 and 2018YFA0702502), the National Natural Science Foundation of China (grant nos. 41974142 and 42074129), National Science Foundation (grant no. EAR-1547228), and Science Foundation of China University of Petroleum, Beijing (grant no. 2462019YJRC005). We also thank the editor-in-chief, J. Etgen, the assistant editor, C. Torres-Verdin, the associate editor, P. Routh, Y. Tang, and two other anonymous reviewers for their constructive and thoughtful comments and suggestions, which have improved the quality of this paper significantly.

DATA AND MATERIALS AVAILABILITY

Data associated with this research are confidential and cannot be released.

APPENDIX A

ADDITIONAL FIGURES

In this section, we provide extra figures to supplement the main body of this paper. Figure A-1 shows profiles from one shot. The shot gather in Figure A-1a is generated by using the acoustic wave equation, whereas the shot gather in Figure A-1b is simulated by

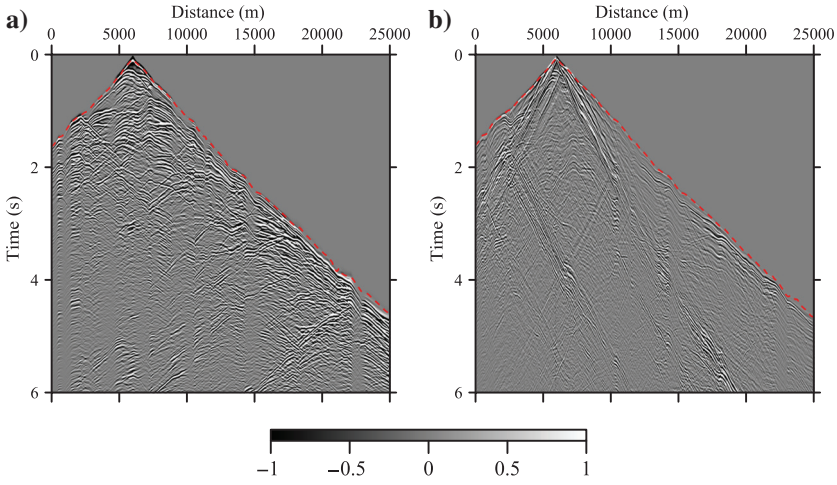

Figure A-1. One shot profile of the (a) acoustic and (b) elastic data sets at a distance of 6 km. The dashed red curves indicate their first breaks.

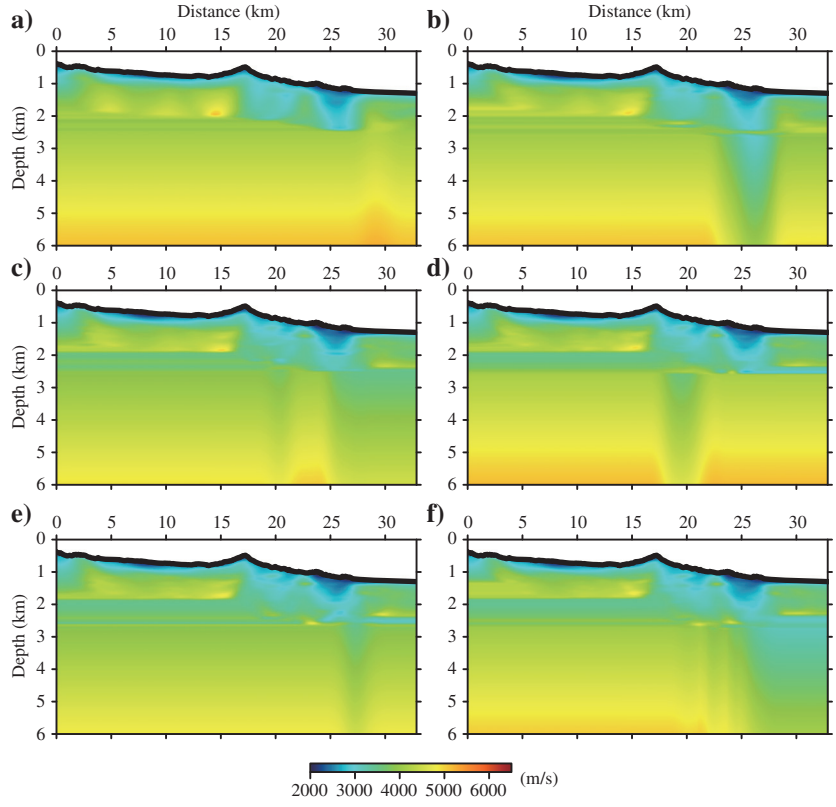

Figure A-2. (a–f) The velocity models generated with ray-based tomography at the 1st, 2nd, 4th, 6th, 8th, and 10th iterations, respectively.

DOI:10.1190/geo2021-0097.1

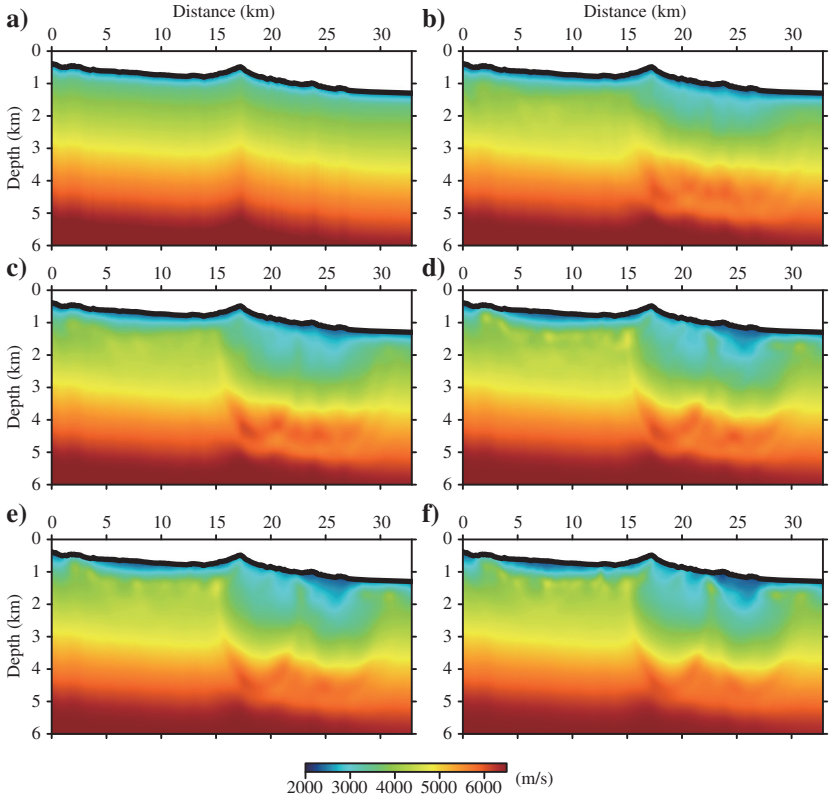

Figure A-3. (a–f) The velocity models produced with WI at the 1st, 10th, 20th, 30th, 50th, and 70th iterations, respectively.

using the elastic wave equation. The S-wave velocity is set as 0.6 times the primary-wave velocity, i.e., $V_S = 0.6V_P$. By comparison, it is clear that the records with different laws of physics have distinct amplitudes and waveforms but share similar first-break time.

The remaining figures demonstrate the model evolution of the third example, which shows a typical model of complex surface and complex geologic structure. Figure A-2 shows the velocity models generated with ray-based tomography at the 1st, 2nd, 4th, 6th, 8th, and 10th iterations, whereas Figure A-3 shows the velocity models produced with WI at the 1st, 10th, 20th, 30th, 50th, and 70th iterations.

REFERENCES

Agudo, Ò. C., N. V. da Silva, M. Warner, and J. Morgan, 2018, Acoustic full-waveform inversion in an elastic world: Geophysics, **83**, no. 3, R257–R271, doi: 10.1190/geo2017-0063.1.

Aki, K., A. Christoffersson, and E. S. Husebye, 1977, Determination of the three-dimensional seismic structure of the lithosphere: Journal of Geophysical Research, **82**, 277–296, doi: 10.1029/JB082i002p00277.

Baeten, G., J. W. de Maag, R.-E. Plessix, R. Klaassen, T. Qureshi, M. Kleemeyer, F. T. Kroode, and Z. Rujie, 2013, The use of low frequencies in a full-waveform inversion and impedance inversion land seismic case study: Geophysical Prospecting, **61**, 701–711, doi: 10.1111/1365-2478.12010.

Bleibinhaus, F., and S. Rondenay, 2009, Effects of surface scattering in full-waveform inversion: Geophysics, **74**, no. 6, WCC69–WCC77, doi: 10.1190/1.3223315.

Borisov, D., F. Gao, P. Williamson, and J. Tromp, 2020, Application of 2D full-waveform inversion on exploration land data: Geophysics, **85**, no. 2, R75–R86, doi: 10.1190/geo2019-0082.1.

Cai, J., H. Wang, J. Chen, Y. Ni, and S. Wang, 2017, Traveltime tomography in the image domain based on the Gaussian-beam-propagator (in Chinese): Chinese Journal of Geophysics, **60**, 3539–3554,

Červený, V., M. M. Popov, and I. Pšenčík, 1982, Computation of wave fields in inhomogeneous media — Gaussian beam approach: Geophysical Journal International, **70**, 109–128, doi: 10.1111/j.1365-246X.1982.tb06394.x.

Chapman, C., J. Hobro, and J. Robertsson, 2010, Elastic corrections to acoustic finite-difference simulations: 80th Annual International Meeting, SEG, Expanded Abstracts, 3013–3017, doi: 10.1190/1.3513472.

Chen, G., W. Yang, S. Chen, Y. Liu, and Z. Gu, 2020, Application of envelope in salt structure velocity building: From objective function construction to the full-band seismic data reconstruction: IEEE Transactions on Geoscience and Remote Sensing, **58**, 6594–6608, doi: 10.1109/TGRS.2020.2978125.

Cheng, X., K. Jiao, D. Sun, Z. Xu, D. Vigh, and A. El-Emam, 2017, High-resolution Radon preconditioning for full-waveform inversion of land seismic data: Interpretation, **5**, no. 4, SR23–SR33, doi: 10.1190/INT-2017-0020.1.

Cobo, Y., C. Calderón-Macías, and S. Chi, 2018, Improving model resolution with FWI for imaging and interpretation in a Gulf of Mexico dataset: 88th Annual International Meeting, SEG, Expanded Abstracts, 1108–1112, doi: 10.1190/segam2018-2997675.1.

Fu, L., and S. M. Hanafy, 2017, Ray-tracing traveltime tomography versus wave-equation traveltime inversion for near-surface seismic land data: Interpretation, **5**, no. 3, SO11–SO19, doi: 10.1190/INT-2016-0210.1.

Graves, R. W., 1996, Simulating seismic wave propagation in 3D elastic media using staggered-grid finite differences: Bulletin of the Seismological Society of America, **86**, 1091–1106.

Gray, S., and K. Marfurt, 1995, Migration from topography: Improving the near-surface image: Canadian Journal of Exploration Geophysics, **31**, 18–24.

Hayashi, K., D. R. Burns, and M. N. Toksöz, 2001, Discontinuous-grid finite-difference seismic modeling including surface topography: Bulletin of the Seismological Society of America, **91**, 1750–1764, doi: 10.1785/0120000024.

Hill, N. R., 2001, Prestack Gaussian-beam depth migration: Geophysics, **66**, 1240–1250, doi: 10.1190/1.1487071.

Hobro, J. W. D., C. H. Chapman, and J. O. A. Robertsson, 2014, A method for correcting acoustic finite-difference amplitudes for elastic effects: Geophysics, **79**, no. 4, T243–T255, doi: 10.1190/geo2013-0335.1.

Hole, J. A., 1992, Nonlinear high-resolution three-dimensional seismic travel time tomography: Journal of Geophysical Research, Solid Earth, **97**, 6553–6562, doi: 10.1029/92JB00235.

Hole, J. A., and B. C. Zelt, 1995, 3-D finite-difference reflection traveltimes: Geophysical Journal International, **121**, 427–434, doi: 10.1111/j.1365-246X.1995.tb05723.x.

Hu, W., 2014, FWI without low frequency data — Beat tone inversion: 84th Annual International Meeting, SEG, Expanded Abstracts, 1116–1120, doi: 10.1190/segam2014-0978.1.

Hu, W., 2016, An improved immersed boundary finite-difference method for seismic wave propagation modeling with arbitrary surface topography: Geophysics, **81**, no. 6, T311–T322, doi: 10.1190/geo2016-0094.1.

Humphreys, E., R. W. Clayton, and B. H. Hager, 1984, A tomographic image of mantle structure beneath Southern California: Geophysical Research Letters, **11**, 625–627, doi: 10.1029/GL011i007p00625.

Jiao, K., D. Sun, X. Cheng, and D. Vigh, 2015, Adjustive full waveform inversion: 85th Annual International Meeting, SEG, Expanded Abstracts, 1091–1095, doi: 10.1190/segam2015-5901541.1.

Komatitsch, D., G. Erlebacher, D. Göddeke, and D. Michéa, 2010, High-order finite-element seismic wave propagation modeling with MPI on a large GPU cluster: Journal of Computational Physics, **229**, 7692–7714, doi: 10.1016/j.jcp.2010.06.024.

Langan, R. T., I. Lerche, and R. T. Cutler, 1985, Tracing of rays through heterogeneous media: An accurate and efficient procedure: Geophysics, **50**, 1456–1465, doi: 10.1190/1.1442013.

Li, X., G. Yao, F. Niu, and D. Wu, 2020, An immersed boundary method with iterative symmetric interpolation for irregular surface topography in seismic wavefield modelling: Journal of Geophysics and Engineering, **17**, 643–660, doi: 10.1093/jge/gxaa019.

DOI:10.1190/geo2021-0097.1

Liu, D. J., J. P. Huang, and Z. Y. Wang, 2020, Convolution-based multi-scale envelope inversion: Petroleum Science, **17**, 352–362, doi: 10.1007/s12182-019-00419-8.

Liu, Y., C. Xie, and J. Yang, 2014, Gaussian beam first-arrival waveform inversion based on Born wavepath: Chinese Journal of Geophysics, **57**, 2900–2909, doi: 10.1002/cjg2.20128.

Liu, Z., and J. Zhang, 2017, Joint traveltime, waveform, and waveform envelope inversion for near-surface imaging: Geophysics, **82**, no. 4, R235–R244, doi: 10.1190/geo2016-0356.1.

Lombard, B., and J. Piraux, 2004, Numerical treatment of two-dimensional interfaces for acoustic and elastic waves: Journal of Computational Physics, **195**, 90–116, doi: 10.1016/j.jcp.2003.09.024.

Lombard, B., J. Piraux, C. Gélis, and J. Virieux, 2008, Free and smooth boundaries in 2-D finite-difference schemes for transient elastic waves: Geophysical Journal International, **172**, 252–261, doi: 10.1111/j.1365-246X.2007.03620.x.

Luo, S., and P. Sava, 2011, A deconvolution-based objective function for wave-equation inversion: 81st Annual International Meeting, SEG, Expanded Abstracts, 2788–2792, doi: 10.1190/1.3627773.

Luo, Y., and G. T. Schuster, 1990, Wave-equation traveltime inversion: 60th Annual International Meeting, SEG, Expanded Abstracts, 1207–1210, doi: 10.1190/1.1889952.

Luo, Y., and G. T. Schuster, 1991, Wave-equation traveltime inversion: Geophysics, **56**, 645–653, doi: 10.1190/1.1443081.

Mei, J., and Q. Tong, 2015, A practical acoustic full waveform inversion workflow applied to a 3D land dynamite survey: 85th Annual International Meeting, SEG, Expanded Abstracts, 1220–1224, doi: 10.1190/segam2015-5850377.1.

Moser, T. J., 1991, Shortest path calculation of seismic rays: Geophysics, **56**, 59–67, doi: 10.1190/1.1442958.

Pratt, R. G., 1999, Seismic waveform inversion in the frequency domain, Part 1: Theory and verification in a physical scale model: Geophysics, **64**, 888–901, doi: 10.1190/1.1444597.

Pyun, S., C. Shin, D.-J. Min, and T. Ha, 2005, Refraction traveltime tomography using damped monochromatic wavefield: Geophysics, **70**, no. 2, U1–U7, doi: 10.1190/1.1884829.

Qin, F., Y. Luo, K. B. Olsen, W. Cai, and G. T. Schuster, 1992, Finite-difference solution of the eikonal equation along expanding wavefronts: Geophysics, **57**, 478–487, doi: 10.1190/1.1443263.

Ramos-Martinez, J., N. Chemingui, S. Crawley, Z. Zou, A. Valenciano, and E. Klochikhina, 2016, A robust FWI gradient for high-resolution velocity model building: 86th Annual International Meeting, SEG, Expanded Abstracts, 1258–1262, doi: 10.1190/segam2016-13872681.1.

Rao, Y., and Y. Wang, 2013, Seismic waveform simulation with pseudo-orthogonal grids for irregular topographic models: Geophysical Journal International, **194**, 1778–1788, doi: 10.1093/gji/ggt190.

Rao, Y., and Y. Wang, 2018, Seismic waveform simulation for models with fluctuating interfaces: Scientific Reports, **8**, 3098, doi: 10.1038/s41598-018-20992-z.

Schuster, G. T., and A. Quintus-Bosz, 1993, Wavepath eikonal traveltime inversion: Theory: Geophysics, **58**, 1314–1323, doi: 10.1190/1.1443514.

Sears, T. J., S. C. Singh, and P. J. Barton, 2008, Elastic full waveform inversion of multi-component OBC seismic data: Geophysical Prospecting, **56**, 843–862, doi: 10.1111/j.1365-2478.2008.00692.x.

Sedova, A., G. Royle, T. Allemand, G. Lambaré, and O. Hermant, 2019, High-frequency acoustic land full-waveform inversion: A case study from the Sultanate of Oman: First Break, **37**, 75–81, doi: 10.3997/1365-2397.n0010.

Shen, X., I. Ahmed, A. Brenders, J. Dellinger, J. Etgen, and S. Michell, 2017, Salt model building at Atlantis with full-waveform inversion: 87th Annual International Meeting, SEG, Expanded Abstracts, 1507–1511, doi: 10.1190/segam2017-17738630.1.

Sheng, J., A. Leeds, M. Buddensiek, and G. T. Schuster, 2006, Early arrival waveform tomography on near-surface refraction data: Geophysics, **71**, no. 4, U47–U57, doi: 10.1190/1.2210969.

Sieminski, A., J.-J. Lévêque, and E. Debayle, 2004, Can finite-frequency effects be accounted for in ray theory surface wave tomography?: Geophysical Research Letters, **31**, L24614, doi: 10.1029/2004GL021402.

Sirgue, L., O. Barkved, J. Dellinger, J. Etgen, U. Albertin, and J. Kommedal, 2010, Thematic set: Full waveform inversion: The next leap forward in imaging at Valhall: First Break, **28**, 65–70, doi: 10.3997/1365-2397.2010012.

Song, C., and T. Alkhalifah, 2020, Wavefield reconstruction inversion via machine learned functions: 90th Annual International Meeting, SEG, Expanded Abstracts, 1710–1714, doi: 10.1190/segam2020-3427351.1.

Spetzler, J., and R. Snieder, 2004, The Fresnel volume and transmitted waves: Geophysics, **69**, 653–663, doi: 10.1190/1.1759451.

Stopin, A., R.-É. Plessix, and S. Al Abri, 2014, Multiparameter waveform inversion of a large wide-azimuth low-frequency land data set in Oman: Geophysics, **79**, no. 3, WA69–WA77, doi: 10.1190/geo2013-0323.1.

Tarantola, A., 1984, Inversion of seismic reflection data in the acoustic approximation: Geophysics, **49**, 1259–1266, doi: 10.1190/1.1441754.

Tarantola, A., 1986, A strategy for nonlinear elastic inversion of seismic reflection data: Geophysics, **51**, 1893–1903, doi: 10.1190/1.1442046.

Tarantola, A., and B. Valette, 1982, Generalized nonlinear inverse problems solved using the least squares criterion: Reviews of Geophysics, **20**, 219–232, doi: 10.1029/RG020i002p00219.

Tromp, J., 2019, Seismic wavefield imaging of Earth's interior across scales: Nature Reviews Earth & Environment, **1**, 40–53, doi: 10.1038/s43017-019-0003-8.

Tromp, J., D. Komatitsch, and Q. Liu, 2008, Spectral-element and adjoint methods in seismology: Communications in Computational Physics, **3**, 1–32.

Tromp, J., C. Tape, and Q. Liu, 2005, Seismic tomography, adjoint methods, time reversal and banana-doughnut kernels: Geophysical Journal International, **160**, 195–216, doi: 10.1111/j.1365-246X.2004.02453.x.

Um, J., and C. Thurber, 1987, A fast algorithm for two-point seismic ray tracing: Bulletin of the Seismological Society of America, **77**, 972–986, doi: 10.1785/BSSA0770030972.

Van Leeuwen, T., and W. A. Mulder, 2010, A correlation-based misfit criterion for wave-equation traveltime tomography: Geophysical Journal International, **182**, 1383–1394, doi: 10.1111/j.1365-246X.2010.04681.x.

Vidale, J., 1988, Finite-difference calculation of travel times: Bulletin of the Seismological Society of America, **78**, 2062–2076.

Virieux, J., and S. Operto, 2009, An overview of full-waveform inversion in exploration geophysics: Geophysics, **74**, no. 6, WCC1–WCC26, doi: 10.1190/1.3238367.

Warner, M., and L. Guasch, 2016, Adaptive waveform inversion: Theory: Geophysics, **81**, no. 6, R429–R445, doi: 10.1190/geo2015-0387.1.

Warner, M., A. Ratcliffe, T. Nangoo, J. Morgan, A. Umpleby, N. Shah, V. Vinje, I. Štekl, L. Guasch, C. Win, G. Conroy, and A. Bertrand, 2013, Anisotropic 3D full-waveform inversion: Geophysics, **78**, no. 2, R59–R80, doi: 10.1190/geo2012-0338.1.

Wong, J., L. Han, J. C. Bancroft, and R. R. Stewart, 2009, Automatic time-picking of first arrivals on noisy micro-seismic data, https://www.crewes.org/ForOurSponsors/ConferenceAbstracts/2009/CSEG/Wong_CSEG_2009.pdf, accessed 26 March 2019.

Woodward, M. J., 1992, Wave-equation tomography: Geophysics, **57**, 15–26, doi: 10.1190/1.1443179.

Wu, R. S., J. Luo, and B. Wu, 2014, Seismic envelope inversion and modulation signal model: Geophysics, **79**, no. 3, WA13–WA24, doi: 10.1190/geo2013-0294.1.

Yang, Y., and B. Engquist, 2017, Analysis of optimal transport and related misfit functions in full-waveform inversion: Geophysics, **83**, no. 1, A7–A12, doi: 10.1190/geo2017-0264.1.

Yao, G., N. V. da Silva, M. Warner, D. Wu, and C. Yang, 2019, Tackling cycle skipping in full-waveform inversion with intermediate data: Geophysics, **84**, no. 3, R411–R427, doi: 10.1190/geo2018-0096.1.

Yao, G., D. Wu, and S.-X. Wang, 2020a, A review on reflection-waveform inversion: Petroleum Science, **17**, 334–351, doi: 10.1007/s12182-020-00431-3.

Yao, J., L. Guasch, M. Warner, T. Lin, and E. Percak-Dennett, 2020b, Geophysical data and gradient translation using deep neural networks: 90th Annual International Meeting, SEG, Expanded Abstracts, 1725–1729, doi: 10.1190/segam2020-3423766.1.

Yong, P., W. Liao, J. Huang, Z. Li, and Y. Lin, 2019, Misfit function for full waveform inversion based on the Wasserstein metric with dynamic formulation: Journal of Computational Physics, **399**, 108911, doi: 10.1016/j.jcp.2019.108911.

Zelt, C. A., and P. J. Barton, 1998, Three-dimensional seismic refraction tomography: A comparison of two methods applied to data from the Faeroe Basin: Journal of Geophysical Research, Solid Earth, **103**, 7187–7210, doi: 10.1029/97JB03536.

Zelt, C. A., and R. B. Smith, 1992, Seismic traveltime inversion for 2-D crustal velocity structure: Geophysical Journal International, **108**, 16–34, doi: 10.1111/j.1365-246X.1992.tb00836.x.

Zhang, W., and X. Chen, 2006, Traction image method for irregular free surface boundaries in finite difference seismic wave simulation: Geophysical Journal International, **167**, 337–353, doi: 10.1111/j.1365-246X.2006.03113.x.

Zhang, Z., Z. Wu, Z. Wei, J. Mei, R. Huang, and P. Wang, 2020, FWI imaging: Full-wavefield imaging through full-waveform inversion: 90th Annual International Meeting, SEG, Expanded Abstracts, 656–660, doi: 10.1190/segam2020-3427858.1.

Zhao, D., A. Hasegawa, and S. Horiuchi, 1992, Tomographic imaging of P and S wave velocity structure beneath northeastern Japan: Journal of Geophysical Research, Solid Earth, **97**, 19909–19928, doi: 10.1029/92JB00603.

Biographies and photographs of the authors are not available.